The Observed Life Cycle of a Baroclinic Instability

WILLIAM J. RANDEL AND JOHN L. STANFORD

Physics Department, Iowa State University, Ames, IA 50010

ABSTRACT

Medium-scale waves (zonal wavenumbers 4–7) frequently dominate Southern Hemisphere summer circulation patterns. Randel and Stanford have studied the dynamics of these features, demonstrating that the medium-scale waves result from baroclinic excitation and exhibit well-defined life cycles. This study details the evolution of the medium-scale waves during a particular life cycle. The specific case chosen exhibits a high degree of zonal symmetry, prompting study based upon zonally averaged diagnostics. An analysis of the medium-scale wave energetics reveals a well-defined life cycle of baroclinic growth, maturity, and barotropic decay. Eliassen–Palm flux diagrams detail the daily wave structure and its interaction with the zonally-averged flow.

1. Introduction

Randel and Stanford (1985, hereafter RS1) have recently studied the dynamics of medium-scale waves (zonal wavenumbers 4–7) in the Southern Hemisphere (SH) summer for a three-year period. This study was motivated by observations that medium-scale waves frequently dominate SH circulation patterns during this season (Salby, 1982; Hamilton, 1983). Randel and Stanford demonstrated that the global circulation patterns vacillate between highly perturbed and zonally symmetric states, and observed clear interactions between the zonal mean flow and the medium-scale waves. An analysis of the medium-scale wave energetics revealed that these waves exhibit well-defined life cycles of baroclinic growth, maturity, and barotropic decay. During these life cycles the characteristics of the medium-scale waves are continually evolving, and the results presented in RS1 were primarily for seasonal statistics and averages; in this paper an individual medium-scale wave life cycle is detailed and discussed.

The results presented here clearly illustrate the evolution of baroclinic waves in the SH summer atmosphere. Distinctive wave structure is observed during the wave growth and decay stages. Several of the characteristics observed, such as the zonal scale selection, eastward phase movement and vertical phase evolution, are similar to those observed of NH·baroclinic waves. This agreement points to the fundamental nature of baroclinic instability in the earth's atmosphere. On the other hand, the particular case detailed here exhibits a high degree of global symmetry not usually observed in NH, and is suggestive of dynamics on a nonlocal scale.
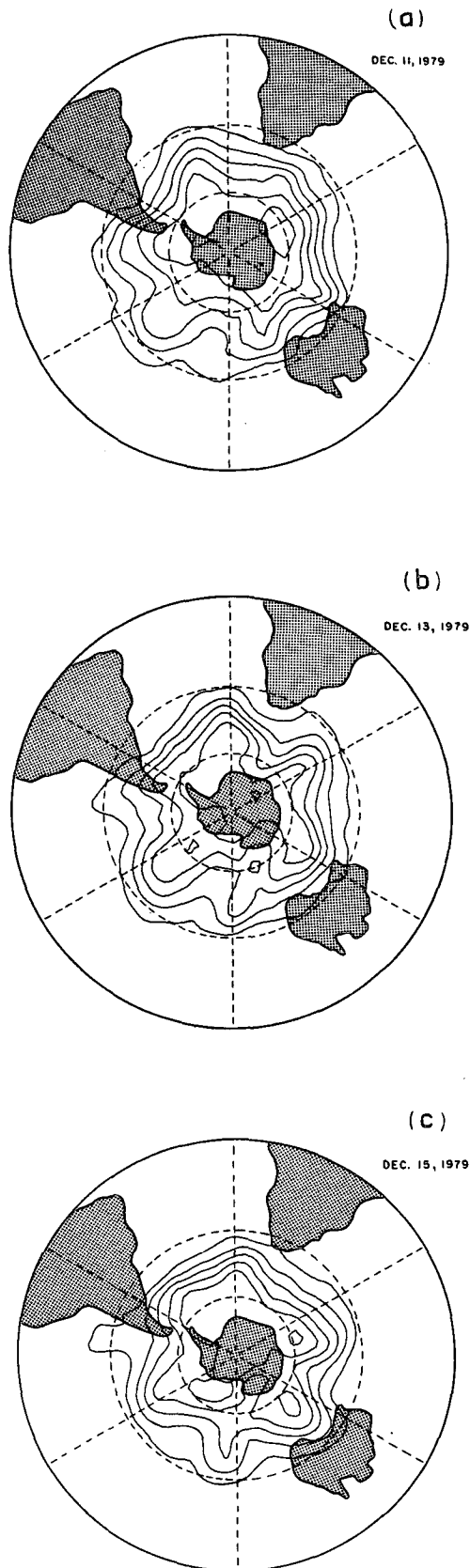
The particular life cycle presented here is compared to modeled nonlinear baroclinic waves reported by Simmons and Hoskins (1978), and the agreement is found to be remarkably good. Comparison with baroclinic waves in laboratory annulus experiments is also discussed.

2. Data and analyses

The data used in this study consist of wind and temperature fields derived from gridded National Meteorological Center (NMC) geopotential height fields, as outlined in RS1. The grids are Fourier analyzed on constant latitude circles to allow convenient partitioning into zonal wavenumber bands. Fourier coefficients of the geostrophic zonal and meridional wind, along with the hydrostatic temperature coefficients, are determined from the geopotential coefficients. The time period covered in this study is 8–17 December 1979, during which time there are no missing data. The date of the peak in wave energy, 13 December 1979, is chosen as day 9 in our study; this is for comparison with the modeled results of Simmons and Hoskins (1978; hereafter HS).

In addition, identical analyses are performed on a separate set of hemispheric grids based on daily operational analyses produced by the Australian Bureau of Meteorology. Temperatures and geopotential heights on eight standard pressure levels (1000–100 mb) are derived from a successive correction analysis that incorporates manual intervention over data sparse areas. Although much of the same atmospheric data are incorporated into both the NMC and Australian schemes, the analysis routines are sufficiently different to provide independent hemispheric grids. Comparison of several derived quantities is made between the two data sets; in general, the agreement is found to be good, although some problems are noted in the Australian analyses above 500 mb. The overall con-

(a)

DEC. 11, 1979

(b)

DEC. 13, 1979

(c)

DEC. 15, 1979

FIG. 1. SH polar stereographic projections of the 200 mb geopotential height contours for three days in December 1979. (a) 11 December, (b) 13 December, (c) 15 December. Contour interval is 200 gpm. Note the sixfold symmetry about the pole each day, and the eastward (clockwise) movement of the patterns with time. Some low latitude contours have been omitted for clarity.

sistency enhances confidence in the results derived from the NMC data. Unless specifically noted, the analyses and discussions presented here are based on the NMC data.

This specific case was chosen because it is apparently a "clean" example of the life cycle which medium-scale waves repeatedly exhibit each year in RS1. Figure 1 displays polar stereographic projections of the 200 mb geopotential height contours on 11, 13, and 15 December 1979. During each of these days a pattern with approximate six-fold symmetry about the South Pole is evident; this is termed a zonal wavenumber 6 pattern. This observed zonal symmetry suggests that the zonally averaged analyses used in this study are physically reasonable, in addition to their analytical and computational advantages. The wave 6 features in Fig. 1 are observed to move eastward (clockwise) in time, at a rate of approximately 7° longitude per day—a phase speed near 6 m s^{-1} in midlatitudes (corresponding to a period near 8–9 days).

The dynamics of these features will be studied here in two ways. First, the latitudinally averaged (over 25–65°S) and vertically integrated (from 850 to 50 mb) (hereafter termed "channel-integrated") wave and zonal mean energy and wave-zonal mean energy exchange are discussed to display the various wave-zonal mean balances. These calculations are based upon the transformed Eulerian-mean formalism of Plumb (1983), outlined in Appendix B of RS1. The channel-integrated wave-zonal-mean energy exchange term is given by:

$$\frac{\partial \bar{E}}{\partial t} = -\frac{\partial E'}{\partial t} = \int dy \int dz$$

$$\times \rho_s \bar{u} \left[\frac{-1}{r \cos^2\theta} \frac{\partial}{\partial \theta} (\cos^2\theta \overline{u'v'}) + \frac{R}{H} f\rho_s^{-1} \frac{\partial}{\partial z} \left(\rho_s \frac{\overline{v'T'}}{N^2} \right) \right]$$

$$= \int dy \int dz \rho_s \bar{u} \cdot DF \quad (1)$$

where $\bar{E}$ is the channel-integrated total zonal mean energy (available potential plus kinetic) and E' is the channel-integrated total wave energy. The quantity DF in Eq. (1) can be written as:

$$DF = \nabla \cdot \mathbf{F}/\rho_s r \cos\theta \quad (2)$$

where $\mathbf{F}$ is the quasi-geostrophic Eliassen-Palm (EP) flux vector:

$$\mathbf{F} = \begin{pmatrix} F_\theta \\ F_z \end{pmatrix} = \rho_s r \cos\theta \begin{pmatrix} -\overline{u'v'} \\ \dfrac{R}{H} f \dfrac{\overline{v'T'}}{N^2} \end{pmatrix}. \quad (3)$$

Energy exchanges due to the first term on the right hand side in Eq. (1) are termed barotropic, while those due to the second are called baroclinic.

The daily wave structure is detailed by means of daily EP flux diagrams for the waves, and cross sections of the zonal mean wind $\bar{u}$ and quasi-geostrophic potential vorticity gradient $\bar{q}_y$. These figures clearly illustrate the evolution of the wave and mean flow throughout this particular life cycle. (For a review of the dynamical information in an EP flux diagram, see Edmon et al., 1980.)

3. Energetics

a. Wave-induced fluxes

Latitude–time series of the wave-induced northward heat flux at 700 mb are shown in Fig. 2, based on NMC data (top) and Australian data (bottom). Good agreement in the time variations for each are observed, with a peak in heat flux near day 9. It is found that
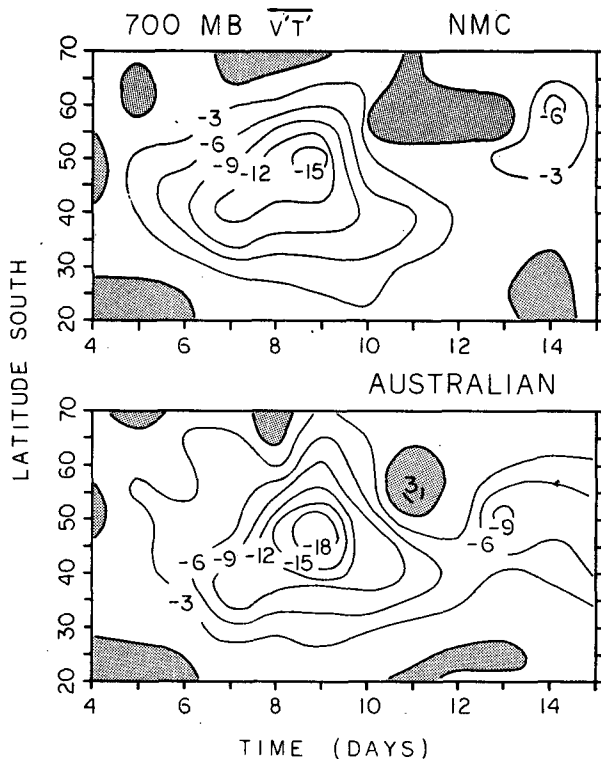

FIG. 3. As in Fig. 2, but for zonally averaged northward momentum flux at 300 mb. Units are m² s⁻².

heat flux variations in the two data sets agree well below 500 mb; above this level the Australian analyses give unrealistic high and low values with little vertical consistency. Similar problems in the Australian analyses above 500 mb were noted by van Loon (1980). An important consequence of this problem is that vertical derivatives of heat flux [as in the baroclinic energy exchange term, Eq. (1)] are quite poor and result in unrealistic values.

Figure 3 shows time variations in the wave-induced northward momentum flux at 300 mb for the NMC data (top) and Australian data (bottom). Good agreement is observed between these data, with a peak in momentum flux near day 10. Unlike the heat flux values discussed above, we find good agreement between the momentum flux values for each data set at all levels throughout the troposphere.

b. Channel-integrated energetics

The channel-integrated energetics over this life cycle are shown in Fig. 4 for both wave 6 alone and waves 5–7 combined. Most of the energy and most of the baroclinic growth are in wave 6 alone. The spectral purity of this baroclinic growth is seen in Fig. 5, where the channel-integrated baroclinic growth rate on 13 December is plotted as a function of zonal wavenumber. The sharp peak at wave 6 shows that

FIG. 2. Latitude–time sections of the zonally averaged northward heat flux at 700 mb for zonal wavenumbers 5–7, based on NMC data (top) and Australian data (bottom). Day 9 is 13 December 1979. Units are K m s⁻¹, with shaded regions denoting equatorward heat flux.

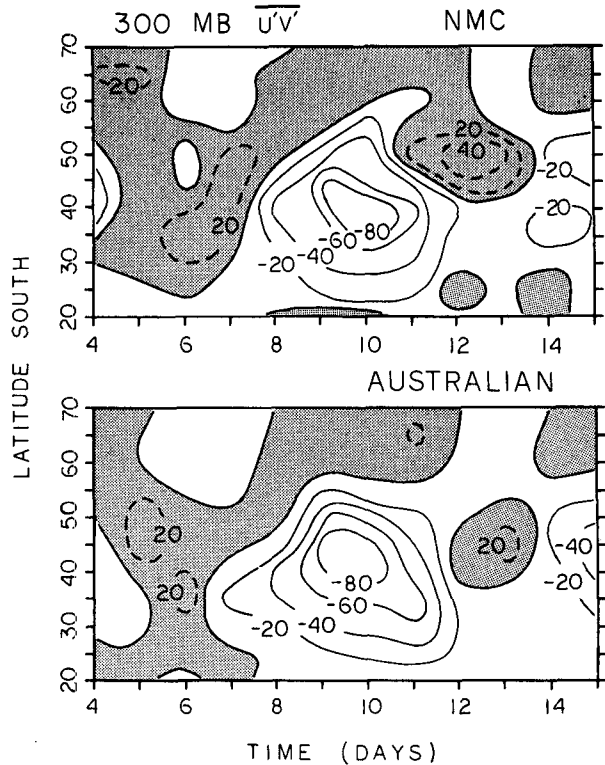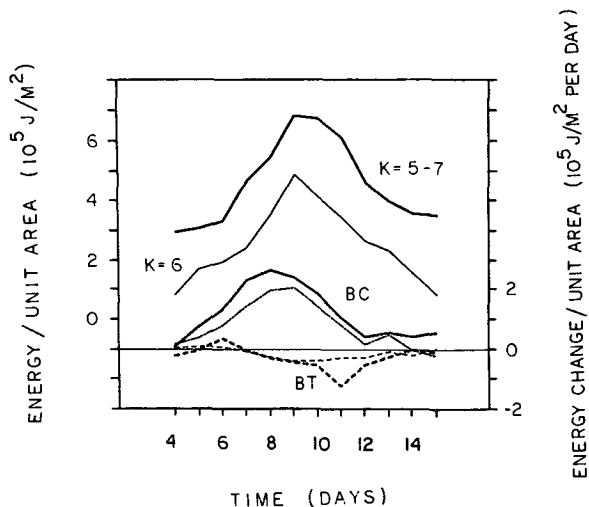FIG. 4. Time variations in channel-integrated energetics during case study. Shown are the wave energy (solid lines), along with the baroclinic (BC) and barotropic (BT) growth terms, for both wave 6 alone (light lines) and waves 5-7 combined (heavy lines). Day 9 is 13 December 1979.

the wave is growing in a zonally symmetric fashion, rather than as a localized feature of the same scale as wave 6. This zonal symmetry is suggestive of a preferred *global* mode for instability, similar to symmetric baroclinic waves observed in laboratory annulus experiments (Pfeffer et al., 1974). Figure 5 also shows the channel-integrated barotropic decay spectrum for 15 December (the data of strongest decay), which is spread over several wavenumbers (predominantly $k = 5-7$), indicating a more longitudinally localized decay. Keeping these facts in mind, we refer to waves 5-7 for the rest of this discussion.

The life cycle (days 5-14) averages of wave energy, along with baroclinic growth and barotropic decay rates, are very similar to SH summer medium-scale wave averages (cf. Tables 1 and 2 and Fig. 15 of RS1). The peak in baroclinic growth precedes the energy peak by one day, whereas the largest barotropic decay occurs approximately two days after the energy maximum. These time lags are in good agreement with the lag-correlation estimates calculated for each of the three summer seasons studied in RS1 (cf. Fig. 11 of RS1). These considerations suggest that the case study detailed here represents a "typical" medium-scale wave life cycle.

The observed energetics (Fig. 4) are in close agreement with the modeled results of HS, shown in Fig. 6. [A concise review of the HS model results can be found in Hoskins (1983). It is worth noting that their model calculations are based on a zonally symmetric wave 6 superimposed upon a zonal mean flow very similar to that observed in the SH summer.] They interpreted this energy cycle as resulting from initial linear baroclinic growth, followed by nonlinear ces-

sation of growth leading to Rossby wave radiation. Latitudinal phase shifts induced in the mature wave by local variations in $\bar{u}$ and $\bar{q}_y$ resulted in barotropic decay of the wave and intensification of the zonally averaged flow.

Similar growth and decay rates are seen in the modeled results (Fig. 6), while the observed maximum decay rate (day 11 of Fig. 4) is roughly one-half as large as the maximum baroclinic growth rate (day 8). (Note that the modeled results include the vertical convergence of momentum flux, which HS note to be a factor of 4 smaller than the horizontal flux. Because of the quasi-geostrophic calculations used here, only the horizontal momentum flux convergence is included in these calculations.) The observed life cycle average growth rate is approximately four times as large as the decay rate. This excess of wave growth is probably not the result of the spectral truncation used here, since contributions from other wavenumbers are observed to be small. Rather, we view this discrepancy as arising from the absence of any dissipation in the energy equations, in addition to uncertainty in the analyses.

The channel-integrated zonal mean energy exhibits compensating energy changes during this period, as shown in Fig. 7. This zonal mean energy change is predominantly due to a reduction in the lower tropospheric temperature gradient, resulting from the poleward heat flux of the waves. This is evident in
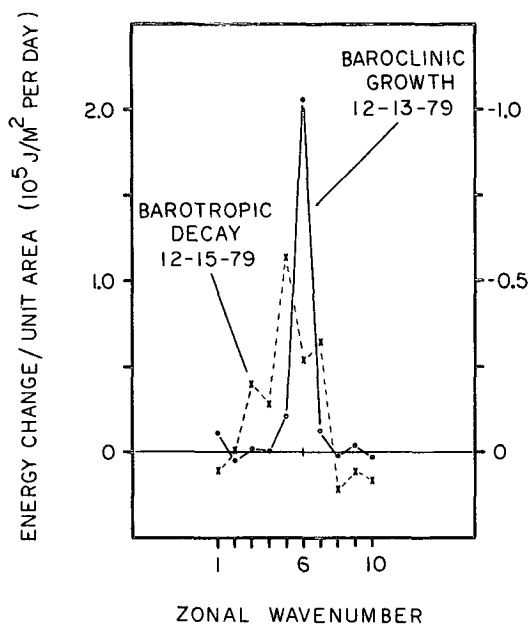

FIG. 5. Zonal wavenumber spectra of the channel-integrated baroclinic growth rate on 13 December 1979 (solid line, left ordinate scale) and barotropic decay rate on 15 December 1979 (dashed line, right ordinate scale). Growth and decay rates are calculated from Eq. (1). Note the sharp peak in baroclinic growth at wave 6.
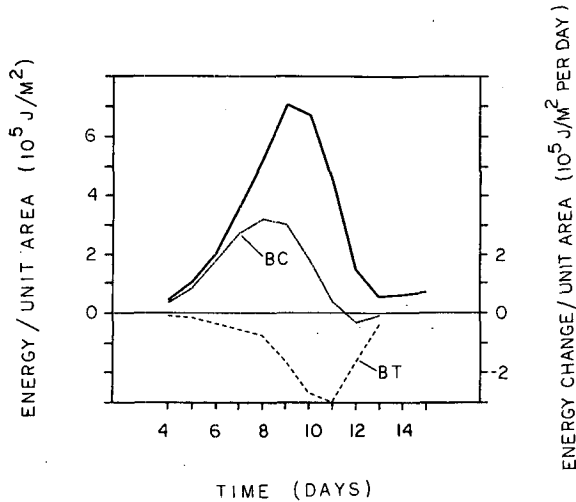
FIG. 6. Life cycle energetics of modeled baroclinic wave, adapted from Simmons and Hoskins (1978). Shown are the wave energy (heavy solid line), along with the baroclinic (BC) and barotropic (BT) growth terms.

4. Daily wave and zonal mean structure

The daily structure and evolution of both the wave and the zonal mean flow are now examined. This discussion is based on the daily EP cross sections (for waves 5–7) shown in Fig. 10, along with daily cross sections of $\bar{u}$ and $\bar{q}_y$ shown in Fig. 11. Plotting conventions for the EP flux diagrams are discussed in Appendix A of RS1. The components of the EP flux vectors are given by Eq. (3), while the contours plotted in Fig. 10 are for the quantity DF given in Eq. (2). The quantity DF (called the wave driving) is related to changes in the zonal wind by the equation:

$$\frac{\partial \bar{u}}{\partial t} = f\bar{v}^* + DF.$$

This shows that zonal mean wind changes are forced by the wave driving term DF, but that the effect of the "residual circulation" $\bar{v}^*$ must also be taken into account. McIntyre (1982) has shown that the residual circulation will generally tend to mitigate the effect of the wave driving, and that actual zonal wind changes will be smaller than those anticipated from DF alone. In addition, DF is proportional to the rate of wave-zonal mean energy exchange, Eq. (1), and equal to the northward flux of quasi-geostrophic potential vorticity, $\overline{v'q'}$ (Palmer, 1982).

Because the daily EP diagrams tend to be rather noisy, a 1-2-1 smoothing filter in latitude is applied to the geopotential Fourier coefficients before further calculations. In addition, some zero contour lines have been omitted for clarity.

The initial jet (day 6) is relatively broad, centered near 35–40°S in the upper troposphere (Fig. 11). The structure of the instability during the first several days shows maximum heat flux in the lowest levels near

Fig. 8, where the zonal mean temperature difference between 30 and 60°S in the upper (200 mb) and lower (850 mb) troposphere over this life cycle is displayed. The 850 mb gradient is weakened as the wave grows, echoing the zonal mean energy change seen in Fig. 7. As discussed in RS1 and Randel (1984), and noted for the modeled results of HS, baroclinic wave growth is most strongly correlated with zonal mean temperature changes in the lower troposphere. For this case study, however, the temperature gradient in the upper troposphere is also modified as the wave evolves. The (reversed) gradient at 200 mb is initially weakened, whereas after a lag of approximately three days it is increased strongly (becoming more negative) as the wave reaches maturity. As will be seen by studying the daily wave structure, this time lag between weakening of the 850 mb gradient and strengthening of the 200 mb gradient can be understood in terms of the upward propagation of the wave as it matures.

Figure 9 displays the channel-integrated energetics based on the Australian data. The zonal mean energy, $k = 5$–7 wave energy, and barotropic energy exchange terms exhibit variations similar to those found in Figs. 4 and 7, which are based on NMC data. A discrepancy between the baroclinic energy exchange term is observed between the two data sets, with the Australian data giving growth rates that are up to a factor of 2 too large. This difference can be traced to the previously discussed erroneous heat flux values derived from the Australian data above 500 mb. In spite of this difference, the overall agreement between the two data sets lends confidence to the NMC-based analyses.
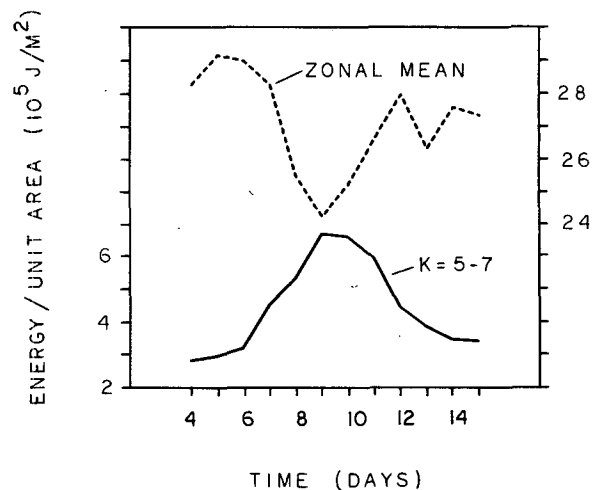

FIG. 7. Time variations in channel-integrated zonal mean and wave energy during case study.
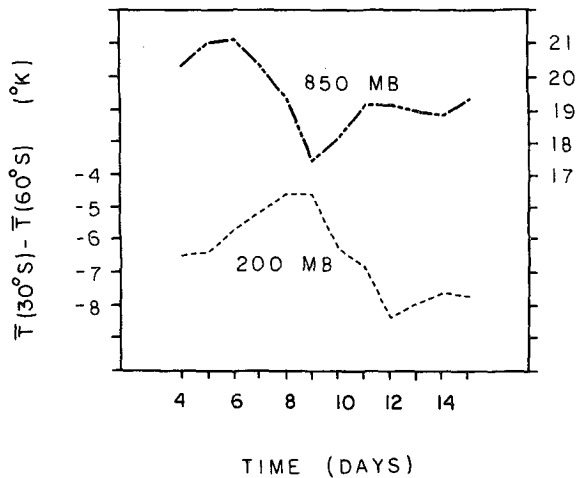
FIG. 8. Zonal mean temperature difference between 30 and 60°S latitude, for 850 mb (top) and 200 mb (bottom), during case study. Note the 200 mb difference *increases* between days 9 and 12.

40–45°S, with predominantly vertical propagation and convergence throughout much of the mid-to-upper troposphere (250–500 mb). As the wave grows, the jet *core* maintains its position and intensity, while the vertical shear in the lower levels over 45–50°S decreases. This results in a much narrower jet by day 9, along with a region of stronger $\bar{q}_y$ below the core. The instability achieves its largest baroclinic growth rate on day 8, with largest (negative) DF in the upper troposphere (200–400 mb) between 30–50°S (Fig. 10). Note that this is the region of largest $\bar{u}$ and $\bar{q}_y$; the wave thereby maximizes both energy generation and downgradient potential vorticity flux (potential enstrophy generation). Note also that a rather vigorous residual circulation $\bar{v}^*$ is implied during this day, since the size of DF in the upper troposphere ($\approx$10 m s^{-1} per day) is substantially larger than observed $\bar{u}$ accelerations ($\approx$1–5 m s^{-1} per day). Moreover, the largest observed changes in $\bar{u}$ occur over a narrower latitudinal (50–60°S) and deeper vertical (100–700 mb) region, as compared to that of DF (30–50°S, 200–400 mb). This behavior is in agreement with the general nature of localized wave forcing, as discussed by McIntyre (1982).

The instability reaches maturity near day 9, with heat flux now extending throughout the entire troposphere (as denoted by the vertical component of arrows in Fig. 10). As a result of this vertical extension, there is less convergence in the upper troposphere, and a slowing of the baroclinic growth rate (which is proportional to the vertical derivative of the poleward heat flux) occurs. During the following days the heat flux lessens in the lower levels, maintaining a maximum in the mid-to-upper troposphere. Note that there is a time lag between maximum heat flux in the lower and upper troposphere; RS1 estimated this

time lag to be on the order of one day. The upper level poleward heat flux results in an increase in the 200 mb zonal mean temperature gradient after day 9, as shown in Fig. 8.

After day 8 the upper level arrows turn increasingly equatorward (Fig. 10). This equatorward propagation is associated with poleward momentum flux and the start of barotropic decay. A large source of positive EP flux divergence (shaded region, Fig. 10) is found in the midtroposphere starting on day 10, associated with the Rossby wave radiation toward the tropics. This leads to positive (upgradient) potential vorticity flux in midlatitudes, centered near 45°S. The barotropic decay and EP flux divergence reach a maximum on day 11. Since the main divergent region on this day (near 45°S) is rather narrow, the latitudinal filtering employed in these figures (but not in the energy calculations) has smoothed the peak value (which is near 12 m s^{-1} per day with no smoothing). A small amount of poleward propagation is also observed during the late stages (days 11–13). The final jet structure is centered near 40–45°S, approximately 5° poleward of the initial state. Comparison with the initial structure shows the final jet to have a more barotropic structure.

The ten-day (life cycle) average EP cross section is shown in Fig. 12. This figure is very similar to the seasonal medium-scale wave averages, shown in Fig. 16 of RS1. This is expected because the seasonal
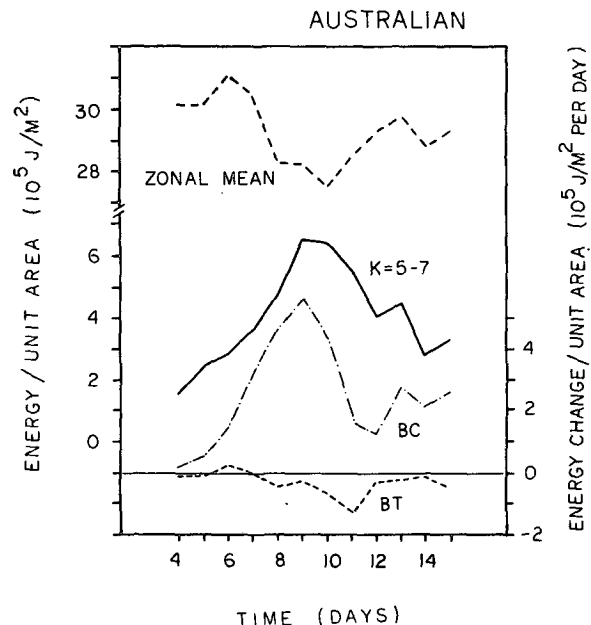

FIG. 9. Time variations in channel-integrated energetics based on Australian data. Shown are the zonal mean and $k = 5$–7 wave energy, along with the $k = 5$–7 baroclinic (BC) and barotropic (BT) growth terms. Compare with energetics based on NMC data in Figs. 4 and 7.
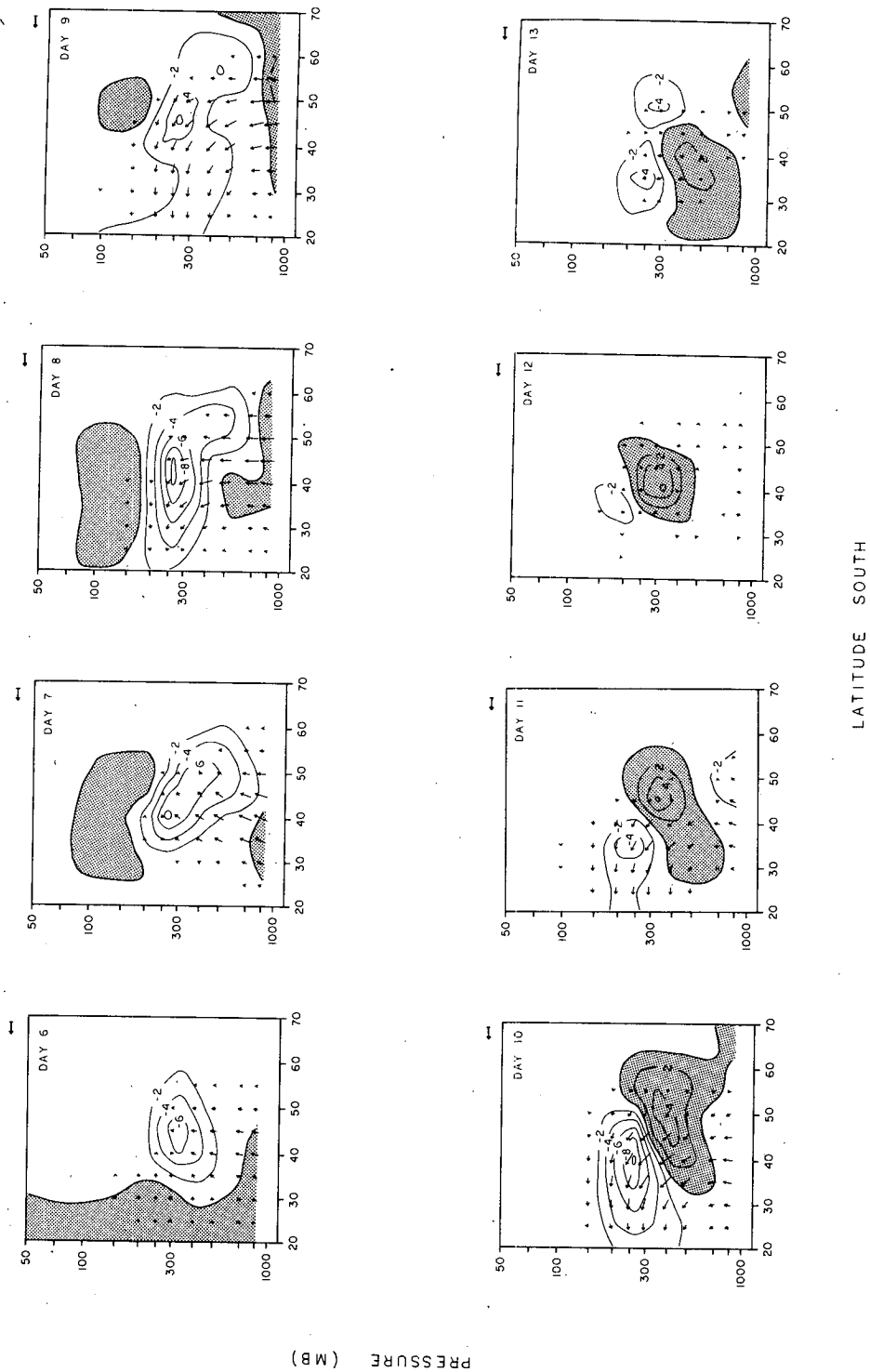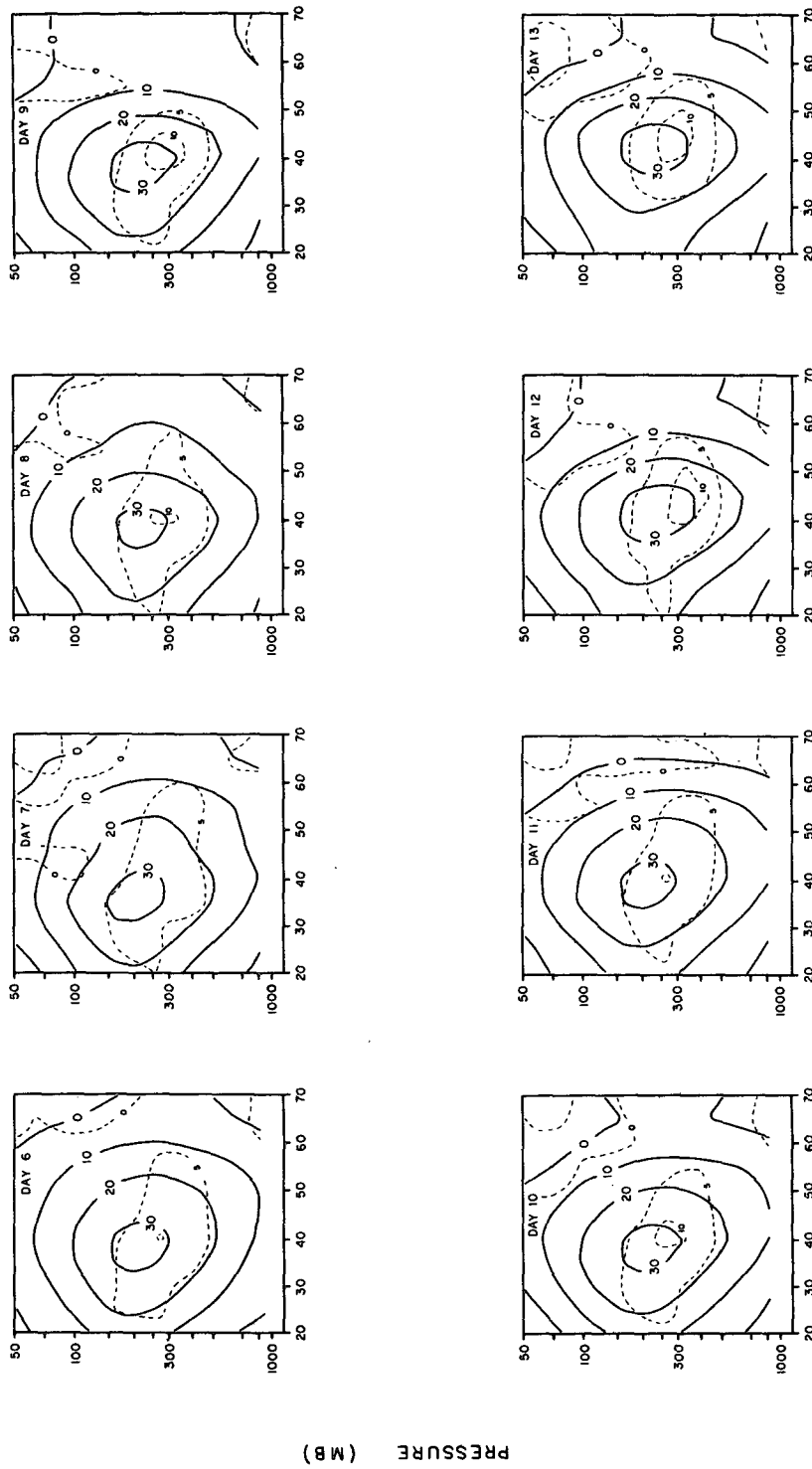
FIG. 10. Daily EP flux diagrams for days 6–13 during case study. Individual days are labeled in the upper right-hand corner. Plotting conventions for the arrows are given in Appendix A of RS1. Contours are of the quantity DF (Eq. 2), with contour intervals of 2 m s^{-1} per day. Shaded regions indicate positive DF.

FIG. 11. Daily cross sections of zonal mean wind (solid lines; contour interval of 10 m s^{-1}) and zonal mean quasi-geostrophic potential vorticity gradient (dashed lines; contour interval of 5 × 10^{-11} (m s)$^{-1}$) for days 6–13 during case study. Individual days are labeled in the upper right-hand corner.
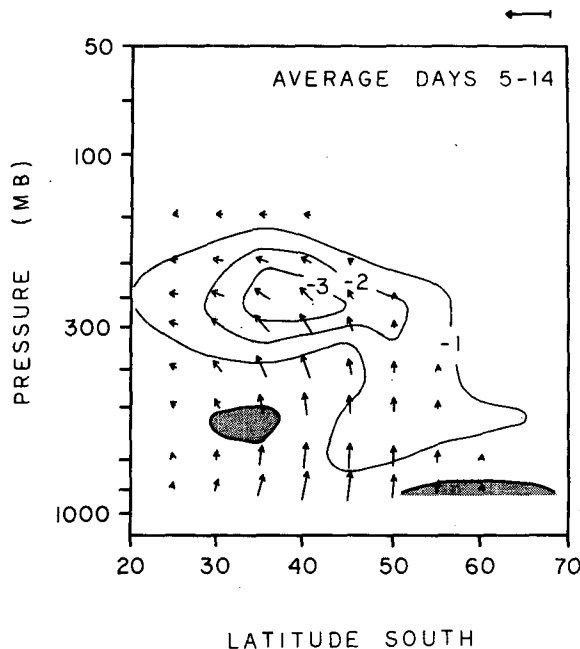
FIG. 12. Life cycle (days 5–14) averaged EP diagram for case study. Plotting conventions as in Fig. 10. Contour intervals are 1 m s⁻¹ per day.

mean is the average over many similar life cycles of medium-scale waves. Note the canceling effects of the negative and positive EP flux divergence in the midtroposphere between growth and decay stages (cf. Fig. 10). It is the residual of this cancellation that appears in the time-averaged picture.

Comparison of these observed cross sections with those of HS is very favorable. Their EP cross sections for day 5 (from Edmon et al., 1980) show similar behavior with the early stages observed here, although their day 8 shows the large divergent region throughout much of the troposphere not observed here until day 10. Their life cycle averaged EP diagram is very similar to Fig. 12. Moreover, their zonal mean jet moves approximately 5° poleward over the life cycle, in agreement with the results here.

Figure 13 shows the evolution of the vertical phase structure of wave 6 at 40°S throughout this episode. The largest phase tilt is below 500 mb for the first several days (in agreement with the low-level heat flux), and is evident throughout much of the troposphere by day 9. A phase difference of 58° (or approximately 1/6 cycle) is observed between 1000 and 200 mb on day 8. This value is in good agreement with the NH winter results of Lau (1979), who showed that geopotential height fluctuations of synoptic temporal scales exhibited a 60° or 1/6 cycle phase tilt between the tropopause and 850 mb levels over regions of enhanced transient wave development, whereas they assumed a more barotropic character away from these regions. A similar situation is ob-

served in Fig. 13, where smaller vertical tilts are evident after day 9. Note that the intense decay stage produces an eastward tilt with height (downward energy propagation) on day 12. Furthermore, Fig. 13 reveals that the phase progression is slower during the growth phase (average of 5.3 m s⁻¹ over days 6–9) as compared to that over the decay stage (average of 8.9 m s⁻¹ over days 9–12). Pfeffer et al. (1974) have noted similar phase velocity variations for baroclinic waves in laboratory annulus experiments. This effect may be due in part to the Doppler shifting of the wave phase speed in the (wave-induced) changing background wind.

5. Summary and discussion

a. Summary: life cycle of a baroclinic wave

In summary, this case study has produced the following picture of the medium-scale, baroclinic wave life cycle: A strong initial zonal mean temperature gradient is associated with a baroclinically growing wave. The wave's poleward heat flux, found initially in the lowest levels, radiates upward, reaching large values in the upper levels several days later. This vertical extension is associated with diminished baroclinic growth rate, while a reduction of the strong meridional temperature gradient in the lower troposphere is associated with smaller heat fluxes there. The wave reaches its largest amplitude approximately one day after its maximum baroclinic growth rate. At maturity, the heat flux is predominantly in the upper levels, and the wave begins propagating strongly equatorward. The barotropic decay reaches a maximum approximately two days following the wave amplitude maximum, resulting in a strengthening of the zonal mean jet. The final jet is more barotropic than that found initially.

b. Discussion

Distinct similarities and differences are found between the medium-scale waves discussed here and
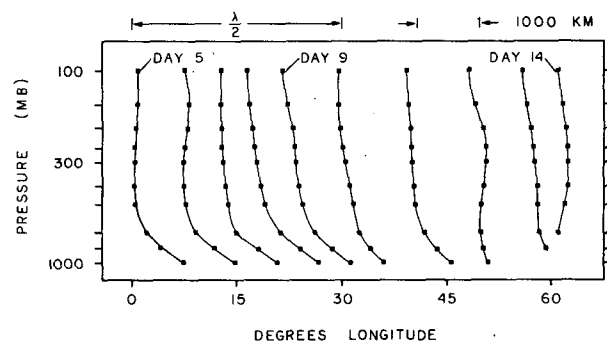

FIG. 13. Daily vertical phase structure for wave 6 at 40°S latitude throughout the case study. Longitudinal scale at bottom along with 1000 km scale for reference.

NH winter transient waves of similar space and time scales. The observed zonal scale ($k = 6$) and eastward phase movement exhibited during this case study are similar to characteristics observed of short period (2.5–6 day) zonally oriented wave trains in the NH winter, which are most clearly identified in "storm track" regions, and are thought to result from baroclinic excitation (Blackmon *et al.*, 1984). In addition, the vertical phase evolution detailed here is in good agreement with NH statistics. These similarities suggest that such characteristics are fundamental to baroclinic instability in the earth's atmosphere, in good agreement with numerous modeling studies.

Interhemispheric differences also point to fundamentally different atmospheric behavior. The most striking difference is that, at times, the SH baroclinic waves occur in a zonally symmetric configuration (as during this case study), whereas their NH counterparts are predominantly observed in localized "storm track" areas [Blackmon, 1976 (NH winter); White, 1982 (NH summer)]. It is important to note that localized behavior is also observed in the SH summer; several clear examples of localized $k = 6$–7 patterns are apparent in the Indian Ocean region in Fig. 3 of Randel and Stanford, 1983. As discussed in RS1, the wave characteristics and energy cycle for these localized features appear similar to those of the global-scale modes, and it is thus unclear if any fundamental dynamical differences exist. The zonal symmetry occasionally observed in the SH summer is undoubtedly related to the relative longitudinal homogeneity of the SH summer atmosphere; the hemisphere may at times act coherently, similar to laboratory annulus experiments. Whatever the cause, the zonal symmetry exhibited in the present case study supports the physical applicability of a zonally averaged analysis, offering a unique opportunity to investigate the associated dynamics. The net result is that the SH summer atmosphere is a good environment for observing the large-scale dynamics of baroclinic instability and a good laboratory for testing theoretical results.

REFERENCES

Blackmon, M. L., 1976: A climatological spectral study of the 500 mb geopotential height of the Northern Hemisphere. *J. Atmos. Sci.* **33**, 1607–1623.

——, Y.-H. Lee and J. M. Wallace, 1984: Horizontal structure of 500 mb height fluctuations with long, intermediate and short time scales. *J. Atmos. Sci.*, **41**, 961–979.

Edmon, H. J., Jr., B. J. Hoskins and M. E. McIntyre, 1980: Eliassen-Palm cross sections for the troposphere. *J. Atmos. Sci.*, **37**, 2600–2616. See also *Corrigendum* **38**, 1115, especially 2nd last item.

Hamilton, K., 1983: Aspects of wave behavior in the mid and upper troposphere of the Southern Hemisphere. *Atmos. Ocean,* **21**, 40–54.

Hoskins, B. J., 1983: Modelling of the transient eddies and their feedback on the mean flow. *Large-Scale Dynamical Processes in the Atmosphere,* B. J. Hoskins and R. P. Pearce, Eds., Academic Press, 169–199.

Lau, N. C., 1979: The structure and energetics of transient disturbances in the Northern Hemisphere wintertime circulation. *J. Atmos. Sci.,* **36**, 982–995.

McIntyre, M. E., 1982: How well do we understand the dynamics of stratospheric warmings? *J. Meteor. Soc. Japan,* **60**, 37–65.

Palmer, T. N., 1982: Properties of the Eliassen-Palm flux for planetary scale motions. *J. Atmos. Sci.,* **39**, 992–997.

Pfeffer, R., G. Buzyna and W. W. Fowlis, 1974: Synoptic features and energetics of wave-amplitude vacillation in a rotating, differentially heated fluid. *J. Atmos. Sci.,* **31**, 622–645.

Plumb, R. A., 1983: A new look at the energy cycle. *J. Atmos. Sci.,* **40**, 1669–1688.

Randel, W. J., 1984: Structure and energetics of medium-scale atmospheric waves in the Southern Hemisphere summer. Ph.D. dissertation, Iowa State University, 171 pp.

——, and J. L. Stanford, 1983: Structure of medium-scale atmospheric waves in the Southern Hemisphere summer. *J. Atmos. Sci.,* **40**, 2312–2318.

——, and ——, 1985: An observational study of medium-scale wave dynamics in the Southern Hemisphere summer. Part I: Wave structure and energetics. *J. Atmos. Sci.,* **42**, 1172–1188.

Salby, M. L., 1982: A ubiquitous wave 5 anomaly in the Southern Hemisphere during FGGE. *Mon. Wea. Rev.,* **110**, 1712–1720.

Simmons, A. J., and B. J. Hoskins, 1978: The life cycles of some non-linear baroclinic waves. *J. Atmos. Sci.,* **35**, 414–432.

van Loon, H., 1980: Transfer of sensible heat by transient eddies in the atmosphere on the Southern Hemisphere: An appraisal of the data before and during FGGE. *Mon. Wea. Rev.,* **108**, 1774–1781.

White, G. H., 1982: An observational study of the Northern Hemisphere extratropical summertime general circulation. *J. Atmos. Sci.,* **39**, 24–40.